Molecular modeling to predict peptide accessibility for peptide-functionalized hydrogels

Xianfeng Li, Jia Jia, Ying Mei, and Robert A. Latour[a)]
Department of Bioengineering, Clemson University, Clemson, South Carolina 29634

(Received 26 June 2017; accepted 7 August 2017; published 18 August 2017)

Peptide-functionalized (PF) hydrogels are being widely investigated by the tissue engineering and regenerative medicine communities for a broad range of applications because of their unique potential to mimic the natural extracellular matrix and promote tissue regeneration. In order for these complex material systems to perform their intended bioactive function (e.g., cell signaling), the peptides that are tethered to the hydrogel matrix must be accessible at the hydrogel surface for cell–receptor binding. The factors influencing the surface accessibility of the tethered peptide mainly include the length of the tethers, the loading (i.e., concentration) of the peptide, and the association between the tethered peptide and the hydrogel matrix. In the present work, the authors developed coarse-grained molecular models based on the all-atom polymer consistent force field for a type of poly(ethylene glycol)-based PF hydrogel and conducted molecular simulations to investigate the distribution of the peptide within the hydrogel and its surface accessibility as a function of tether length and peptide concentration. The calculated results of the effects of these design parameters on the surface accessibility of the peptide agree very well with corresponding experimental measurements in which peptide accessibility was quantified by the number of cells attached to the hydrogel surface per unit area. The developed modeling methods are able to provide unique insights into the molecular behavior of PF hydrogels and the distribution of the tethered peptides, which can serve as a guide for hydrogel design optimization. © *2017 American Vacuum Society*. [http://dx.doi.org/10.1116/1.4992101]

I. INTRODUCTION

Peptide-functionalized (PF) hydrogels are synthetic biomaterials containing low concentrations of bioactive peptides that are covalently tethered to the hydrogel matrix. PF hydrogels represent the most widely used material system in tissue engineering and regenerative medicine applications because of their potential to mimic the extracellular matrix and direct cellular response.[1–7] A typical PF-hydrogel system is composed of a polyethylene-glycol (PEG)-based matrix tethered with bioactive amino-acid sequences, such as arginine–glycine–aspartic acid (RGD). The PEG matrix is nonionic and highly hydrophilic and generally provides a high degree of biocompatibility for many soft-tissue applications. The matrix itself is inherently resistant to nonspecific cell adhesion and protein adsorption, with the tethered bioactive peptides providing the potential for cell signaling to direct a specific cellular response. The RGD amino-acid sequence is one of the most widely used cell-adhesion-promoting peptides, which has been found in numerous extracellular matrix proteins, including collagen I, fibronectin, fibrinogen, and vitronectin.[8–11]

In order for PF hydrogels to function as desired, it is essential that the bioactive peptides contained within the hydrogel matrix are presented in a manner that provides for their accessibility (or bioavailability) at the hydrogel surface for cell–receptor binding. For example, if the tether is too short, the peptide may not be available at the hydrogel surface.[12] Alternatively, if the tether is too long or too strongly associated with the hydrogel matrix, the peptide may be trapped within the hydrogel, again limiting its availability for cell signaling. While bioactivity can be experimentally probed for different hydrogel compositions and designs by an appropriate set of assays, experimental methods alone are limited in their ability to interpret the molecular basis for measured differences in bioactivity. Due to this limitation, bioactive hydrogel systems have often been optimized using trial-and-error approaches. While effective, such trial-and-error approaches are limited in their ability to identify optimal hydrogel designs because the design space for these complex materials is enormously large. In contrast, molecular modeling and simulation methods hold the remarkable potential to understand, visualize, and predict the behavior of tethered peptides within a hydrogel network and how the properties of bulk hydrogels, linkers, and peptides affect peptide accessibility individually or by combinations. Since molecular models of PF hydrogels have not been previously developed, the objective of this research was therefore to develop molecular simulation methods to provide this capability and demonstrate their ability to serve as a powerful tool for PF-hydrogel design to optimize their bioactivity for the biomaterials community.

A number of molecular modeling studies on crosslinked polymer networks have been reported over the last couple decades.[13–31] A review of these studies was given in Ref. 28. Numerical schemes have also been developed specifically for PEG-based systems. Examples include the studies of conformation and hydrodynamics of PEG,[32] the interfacial

[a)]Electronic mail: latourr@clemson.edu

properties of PEG surfactant/water,[34,35] PEG-contained proton-exchange membranes,[22] PEG-contained lipid systems,[33] and the development of kinetic models to predict growth, crosslink density profiles, and the level of ligand incorporation for PEG hydrogels.[36] Recently, molecular simulations were conducted to study the behavior of an individual peptide–polymer conjugated construct composed of a peptide sequence of four phenylalanine amino acid residues linked to a single 100-mer PEG chain to examine the influence of the polymer backbone on the conformation of a tethered peptide.[37] None of these previous studies, however, have used molecular modeling methods to simulate and predict the behavior of a tethered peptide sequence within a crosslinked hydrogel matrix, let alone the availability of a tethered peptide for cell–receptor binding, which is essential for cell signaling.

While previous molecular modeling studies have been reported for crosslinked polymers and hydrogels using all-atom (AA) models,[13–17] coarse-grained (CG) models,[18–23] and lattice models,[24–27] each of these individual methods has its own limitations. In modeling, the crosslinking process is typically modeled as a collision process in which crosslinking happens when two linkable chain ends meet. Due to slow diffusion of chain segments in a densely entangled environment, molecular dynamics (MD) methods based on AA and even CG models are very difficult to generate and equilibrate models of crosslinked polymer networks at experimental densities for direct comparison with experimental systems. And, while lattice-model methods provide an efficient approach for constructing crosslinked polymer-network densities matching experimental systems, the restrictions of the lattice (such as lack of atomic detail, artificial discrete degrees of freedom and the short range and isotropic nature of the interactions[38]) result in physically unrealistic structural distortions of the network. To overcome the individual limitations of each method on its own, we recently developed and validated a modeling toolset designed specifically for the simulations of PF hydrogels.[39] The toolset consists of three consecutive parts: (1) building a global crosslinked PF hydrogel network using a "guided" lattice model based on Monte Carlo (MC) methods, (2) recovering the local molecular structure of the network by transitioning from the lattice model to an off-lattice CG model, and (3) recovering an AA structure of the PF hydrogel network by reverse mapping from the CG structure.

The CG force field is the core component bridging models at these different time and length scales. In this work, we have parameterized the CG model of a class of PEG-based hydrogels with different lengths of pendant arms (i.e., tethers) presenting an RGD sequence. The CG parameter library was developed based on the polymer consistent force field (PCFF).[40–43] Combined with the CG force field and the multiscale modeling toolset, we constructed molecular models of RGD-functionalized PEG-based hydrogels and analyzed the dependence of the accessibility of the RGD peptide at the hydrogel surface on the length of tether linking the peptide to the hydrogel matrix and the peptide loading (i.e., concentration) within the hydrogel matrix. To evaluate the performance of the simulation methods, we compared the simulation results with corresponding experimental measurements given by Jia *et al.*[12] for the accessibility of the RGD segments at the surface of these same PEG-based PF hydrogels as determined by cell-binding density. The simulation results were further analyzed to provide information on the predicted average orientation of peptide at surface and the critical surface density of the peptide needed to maximize cell adhesion to the hydrogel surface, which we propose to also be important design parameters for the optimization of PF-hydrogel bioactivity.

II. MATERIALS

For a given PEG-based PF hydrogel system, the tether length, peptide concentration, and the association between the tethered peptide and the hydrogel matrix are the primary factors influencing the accessibility of the tethered peptides at the hydrogel surface. To examine the effect of these factors and compare our modeling results with corresponding experimental results given by Jia *et al.*,[12] we constructed molecular models of PF-hydrogel with a similar set of design conditions that were used in the experimental work. The PEG-based PF-hydrogels that were studied in this work contain two types of crosslinkable monomers, as shown in Fig. 1. The matrix of the hydrogel was composed of poly(ethylene glycol) diacrylates (PEGDA) with 700 Da molecular weight (corresponding to $n = 12$ in Fig. 1). The tethered peptide sequence was Arg-Gly-Asp-Ser-Pro (RGDSP). The N-terminal of the peptide was linked by a series of Gly (G) segments to a methacrylate tether, by which the peptide was attached to the PEGDA matrix. The number ($m = 2$, 4, and 6) of Gly linkers between the peptide and the methacrylate (i.e., G_2, G_4, and G_6) controls the length of the tether. The ratio of the two types of crosslinkers can be varied precisely by controlling the stoichiometry during hydrogel synthesis to achieve different peptide concentrations within the hydrogel matrix. In this study, we modeled nine concentrations of the peptide (1.7, 3.4, 5.1, 6.8, 8.5, 10.2, 11.9, 13.6, and 15.3 mM), each with three different tether lengths (G_2, G_4, and G_6), thus generating 27 different hydrogel systems in all.

III. SIMULATION METHODS

A. Coarse-grained method

All simulations were conducted using a three-step multiscale modeling toolset developed in house. The details of the lattice, CG, and AA methods in each step of the toolset were introduced in a previous paper.[39] In a coarse-graining process,[44,45] several atoms are grouped together and represented by a bead with the mapping point being taken as the center of mass of each group of atoms. Figure 1 illustrates the strategy used to coarse-grain the two types of crosslinkers (PEGDA and MethG_mRGDSP) and the copolymer network formed by them. This CG strategy includes ten types of beads, labeled as A, B, C, D, E, F, G, P, R, and S (Table I), 14 types of bonds (Table II), 20 types of bond angles (Table

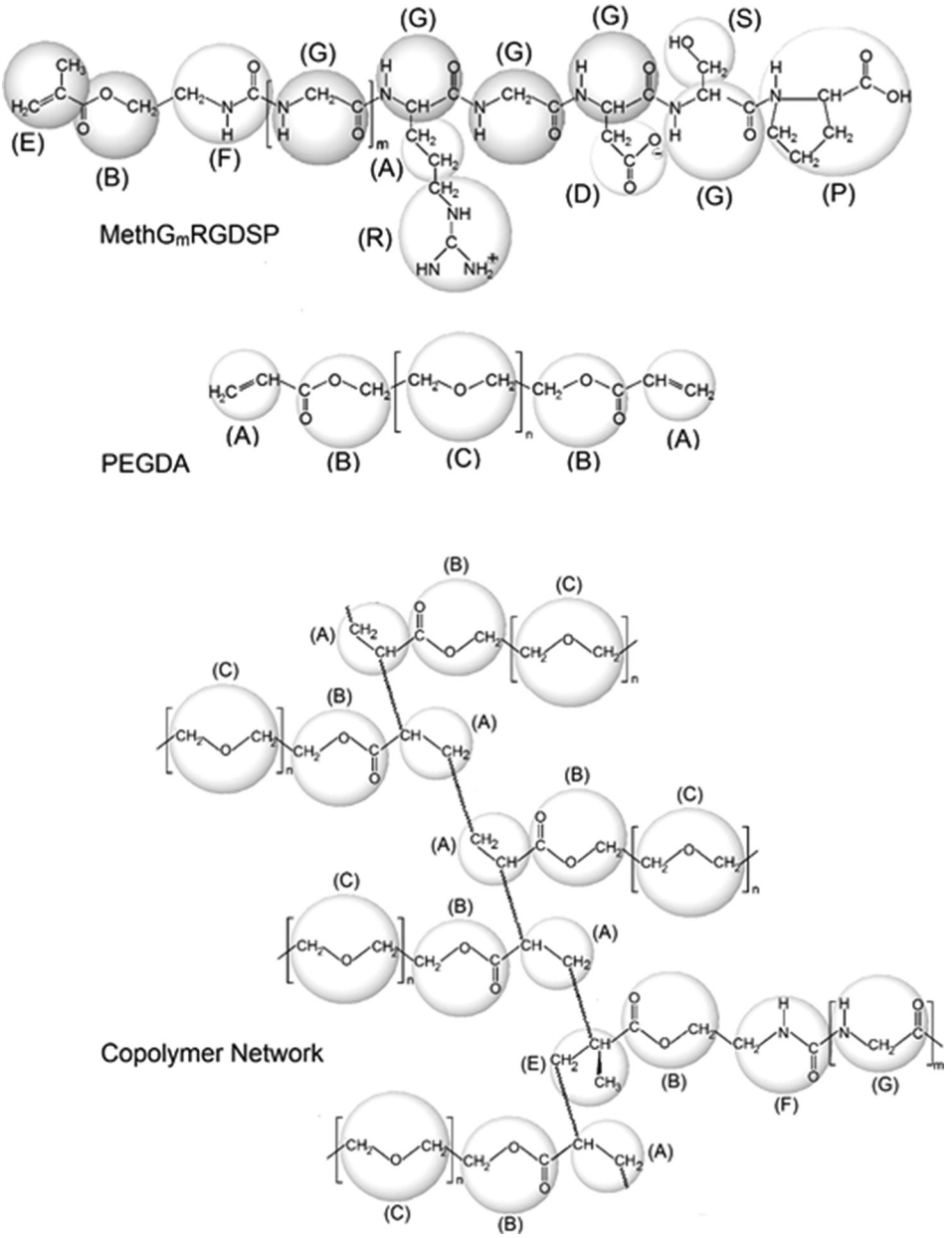

FIG. 1. Schematic representation of the coarse gaining strategy for MethG$_m$RGDSP (m = 2, 4, and 6) and PEGDA (n = 12) crosslinkers and the copolymer network formed by them.

III), and 29 types of dihedral angles (Table IV). In addition, similar to the Martini CG force field,[46] the water molecules are also represented by a CG scheme, in which four atomic waters are represented by one single bead. Therefore, there are two more types of CG bead, WP4 and BP4 (Table I), used to represent water and antifreeze molecules, respectively,[46,47] as addressed in Sec. IV A. The potential terms that needed to be parameterized included bonded terms for bond stretching (E_{stretch}), bond-angle bending (E_{bend}), and bond rotation (E_{torsion}), and a nonbonded term represented by van der Waals (vdW) interactions (E_{vdW}). For each interaction term, the CG parameters were derived using the iterative Boltzmann inversion of the corresponding atomistic distribution functions obtained from AA MD simulations of

TABLE I. Ten types of CG beads and their associated PCFF parameters for the van der Waals interactions in the CG model of the hydrogel network formed by the PEGDA and MethGmRGDSP crosslinkers shown in Fig. 1. The parameters are defined in Eq. (4). The WP4 and BP4 types represent the water and antifreeze CG beads (Ref. 45), respectively.

Bead type	σ (Å)	ε (kcal/mol)	Bead type	σ (Å)	ε (kcal/mol)
A	4.6000	0.1510	**G**	4.8000	0.6964
B	4.0000	0.2907	**P**	5.8000	0.2973
C	4.6000	0.2051	**R**$^{(+1)a}$	5.5000	1.3961
D$^{(-1)a}$	4.7000	1.0260	**S**	4.4000	0.1000
E	5.2000	0.6036	**WP4**	4.7000	1.1950
F	4.8000	0.6964	**BP4**	5.7000	1.3384

[a]The charges for **R** and **D** are included as superscript.

TABLE II. Bond-length types and PCFF parameters for the bonding interactions in the CG model of the hydrogel network formed by the PEGDA and $MethG_mRGDSP$ crosslinkers shown in Fig. 1. The parameters are defined in Eq. (1).

Bond type	l_c (Å)	K_b (Å^{-2})	Bond type	l_c (Å)	K_b (Å^{-2})
A–A	2.5945	23.5808	**B–F**	3.4169	17.8277
A–B	3.0922	69.3101	**C–C**	3.6471	66.3255
A–E	2.6274	23.7812	**D–G**	2.6273	113.9367
A–G	2.7314	163.7079	**F–G**	3.5098	13.0061
A–R	3.7013	11.0207	**G–G**	3.2098	13.0061
B–C	3.5687	56.1082	**G–P**	3.6862	102.2745
B–E	3.1484	40.5811	**G–S**	2.1354	119.6280

small structure units immersed in explicit water using the PCFF TIP3P water model.[48] During the iterative procedure for a particular distribution, the rest of the potentials were kept constant. According to the suggestion of Reith *et al.*,[49] the potential terms were optimized in a descending order of their relative strength, with parameterization thus systematically developed in the order of $E_{\text{stretch}} \rightarrow E_{\text{bend}} \rightarrow E_{\text{vdW}} \rightarrow E_{\text{torsion}}$.

For each bonded interaction term, the CG parameters were derived by mapping the structure distribution functions obtained from MD simulations of each of the 4-mer segments (Fig. 1 and Table IV) represented in the hydrogel structure immersed in explicit waters represented by CG and AA models. The probability distributions of bond lengths and bond angles were first fitted by a Gaussian function, which were then Boltzmann-inverted to provide the potential equations of bond stretching and bond-angle bending. In this way, the bond stretching and angle bending potentials were computed by

$$E_{\text{stretch}}(l) = k_B T K_b (l - l_c)^2, \tag{1}$$

$$E_{\text{bend}}(\theta) = k_B T K_\theta (\theta - \theta_c)^2, \tag{2}$$

where l and θ are bond length and angle, and k_B and T are the Boltzmann's constant and temperature, respectively, and (l_c, K_b) and (θ_c, K_θ) are parameter sets obtained from the fitting of the bond-length and bond-angle distributions, respectively. The torsional potential was then calculated by a threefold Fourier progression formula, i.e.,

$$E_{\text{torsion}}(\phi) = \sum_{n=1}^{3} K_n [1 + \cos(n\phi - \delta_n)], \tag{3}$$

where ϕ is the dihedral angle, and K_n and δ_n are force constants and phase angles, respectively.

Finally, the nonbonded vdW interactions were represented by the Lennard-Jones 9–6 potential form that is used in the PCFF force field[40–43]

$$E_{VDW} = \varepsilon_{ij} \left[2 \left(\frac{\sigma_{ij}}{r_{ij}} \right)^9 - 3 \left(\frac{\sigma_{ij}}{r_{ij}} \right)^6 \right], \tag{4}$$

where ε_{ij} is the depth of the potential well, σ_{ij} is the vdW radius that corresponds to r_{ij} when E_{vdW} is at its minimum value, and r_{ij} is the distance between a pair of CG beads. The parameterization of the vdW interactions were conducted by an inverted Boltzmann method[50,51] in which a numerical potential was determined iteratively by matching the radial distribution functions (RDF) obtained from CG and AA models for each type of CG bead unit. To parameterize the vdW interactions, we developed and equilibrated AA models of aqueous solution (10 wt. % solute; approximate composition of experimentally synthesized hydrogels[52]) for each type of low molecular weight compound that has similar chemical structure as the corresponding superatom entity defined in the CG model (Fig. 1). The parameters ε and σ for the same-type CG beads were then obtained by mapping the RDF obtained from the CG model to the RDF of the equivalent AA models. For unlike bead pairs i and j, we then used a sixth-order combining rule, which is conventionally used in PCFF (Refs. 39, 40, and 53) to calculate the off-diagonal parameters

$$\varepsilon_{ij} = 2\sqrt{\varepsilon_i \varepsilon_j} \frac{\sigma_i^3 \sigma_j^3}{\sigma_i^6 + \sigma_j^6}, \quad \text{and} \quad \sigma_{ij} = \left(\frac{\sigma_i^6 + \sigma_j^6}{2} \right)^{1/6}. \tag{5}$$

It is noted that CG beads **R** and **D** represent the side chains of arginine (Arg) and aspartic acid (Asp), which are positively (+1) and negatively (−1) charged, respectively. For nonbonded interactions between same or different types of charged bead pairs, the current nonbonded interaction parameterization procedure includes both van der Waals and the electrostatic interactions. Specifically, when we mapped the RDFs calculated from CG models onto those calculated from AA models for the charged beads, we adjusted not only the parameters σ and ε but also the dielectric constant to get best mapping results (see Sec. IV A). The vdW parameters for the CG bead representing water were obtained based on the Martini CG parameters for water.[46,47] Specifically, we used the RDF profile of CG water calculated based on Martini force field as a target, and the Martini nonbonded parameter pairs of σ and ε for water as an initial guess, and

TABLE III. Bond-angle types and PCFF parameters for the angle bending interactions in the CG model of the hydrogel network formed by the PEGDA and $MethG_mRGDSP$ crosslinkers shown in Fig. 1. The parameters are defined in Eq. (2).

Angle type	θ_c (deg)	K_θ (rad^{-2})	Angle type	θ_c (deg)	K_θ (rad^{-2})
A–A–A	130.6700	1.7831	**B–F–G**	117.6800	60.7375
A–A–B	122.7000	0.5978	**C–C–C**	111.4200	22.0420
A–A–E	149.6000	1.2780	**D–G–G**	142.2000	52.2008
A–B–C	112.5000	14.2565	**E–B–F**	96.2060	69.7375
A–E–A	112.6400	1.2320	**F–G–G**	98.1360	30.2560
A–E–B	128.1800	23.5418	**G–A–R**	115.7500	16.5279
A–G–G	117.0200	57.0903	**G–G–G**	101.1326	30.2560
A–G–F	117.0200	57.0903	**G–G–P**	134.9500	24.7632
B–A–E	151.1500	9.8460	**G–G–S**	111.7200	114.7766
B–C–C	121.8400	11.1981	**P–G–S**	112.6200	27.1179

TABLE IV. Dihedral-angle types and PCFF parameters for the torsional interactions in the CG model of the hydrogel network formed by the PEGDA and MethG_mRGDSP crosslinkers shown in Fig. 1. The parameters are defined in Eq. (3).

Dihedral type	K_1 (kcal/mol)	K_2 (kcal/mol)	K_3 (kcal/mol)	δ_1 (deg)	δ_2 (deg)	δ_3 (deg)
A–A–A–A	0.0500	−0.0600	0.0300	0	0	0
A–A–A–B	−0.0500	−0.0600	−0.0300	0	0	0
A–A–A–E	0.0500	−0.2100	0.1300	0	0	0
A–A–B–C	0.9000	−0.1400	0.0300	0	0	0
A–A–E–A	−0.3800	−0.0100	0.0000	0	0	0
A–A–E–B	−0.2700	0.1200	−0.0200	0	0	0
A–B–C–C	1.5700	0.1700	−0.0800	0	0	0
A–E–A–B	−0.4700	−0.3700	−0.2300	$\pi/3$	0	0
A–E–B–F	−0.9500	−0.6400	−0.1700	$\pi/3$	0	0
A–G–F–B	1.9100	−0.0300	0.8100	0	0	0
A–G–G–F	−0.2400	1.1100	−0.4000	$\pi/3$	$\pi/3$	0
A–G–G–G	−0.2400	1.1100	−0.4000	$\pi/3$	$\pi/3$	0
B–A–A–B	−1.0000	0.3700	−0.0100	0	0	0
B–A–A–E	0.3000	−0.0700	−0.0400	0	0	0
B–A–E–B	0.1900	−0.0800	−0.0600	0	0	0
B–C–C–C	0.0500	−0.7000	−0.6500	$\pi/3$	0	0
B–F–G–G	−1.1500	0.3400	0.4100	0	0	0
C–B–A–E	0.0900	−0.1400	0.0300	0	0	0
C–C–C–C	0.9000	0.0400	−0.4500	0	0	0
D–G–G–G	1.9800	1.1600	−0.4200	0	0	0
D–G–G–P	2.0000	0.8700	0.0100	0	0	0
D–G–G–S	−1.4700	2.010	−0.9400	0	0	$2\pi/3$
E–B–F–G	1.9900	−0.0700	−0.2600	0	0	0
F–G–A–R	2.0100	−1.9800	−1.4900	$\pi/3$	$\pi/3$	0
F–G–G–G	0.2200	0.4100	−0.5800	0	0	0
G–G–A–R	2.0100	−1.9800	−1.4900	$\pi/3$	$\pi/3$	0
G–G–G–G	0.2200	0.4100	−0.5800	0	0	0
G–G–G–P	0.2800	−1.9900	1.2200	0	$2\pi/3$	$2\pi/3$
G–G–G–S	−1.5700	−1.1900	−0.7600	0	$\pi/3$	0

then modified the value of ε in our calculations based on PCFF until the RDF of CG water calculated based on PCFF matched the target Martini profile. Note that when mapping to all-atom simulation results of RDF, the vdW parameters σ and epsilon are difficult to determine unambiguously since multiple pairs may perform similarly well (e.g., bigger R and smaller epsilon give similar vdW interactions). We therefore used the similar water CG model as that defined in the Martini method, and chose to use the same σ and only adjusted the value of ϵ based on PCFF.

B. Simulation setup

The CG model of the hydrogel network composed of PEGDA and MethG_nRGDSP includes 29 types of dihedrals in total. To parameterize the bonded interactions including bond-stretching, bond-angle-bending, and bond–rotation interactions, we constructed AA and corresponding CG models of aqueous solutions of 29 types of 4-mer conformers. Each 4-mer conformer represented four successively connected units in the coarse-graining strategy presented in Fig. 1. For the AA models of aqueous solutions of the 4-mer conformers, each model contained one conformer type capped with methyl groups at each end. A 60-ns MD simulation was then conducted for each conformer system represented by the AA and CG models in a cubic box with dimensions $24 \times 24 \times 24$ Å^3. Periodic boundary conditions were applied in all dimensions. The resulting probability distribution plots for each bond type were then used along with Eqs. (1)–(3) for the fitting of the CG parameters for bond-stretching, bond-angle-bending, and bond–rotation interactions, respectively.

The CG model of water is similar to the standard Martini water model, in which one CG bead represents four atomistic water molecules and is charge neutral. To parameterize the nonbonded vdW interaction, a water box containing 535 CG beads was built with $40 \times 40 \times 40$ Å^3 dimensions and periodic boundary condition. The vdW parameter σ was fixed to be 4.7 Å, which is the same as the value in the standard Martini force field,[46] and the parameter ε was adjusted to match the calculated RDF onto the corresponding result obtained in Ref. 47.

To parameterize the nonbonded vdW interactions for the ten types of beads forming the PF-hydrogel network, we developed AA models of aqueous solutions of low molecular weight compounds that had similar chemical structure as each type of bead defined in the CG model (Fig. 1). The AA models of aqueous solution containing 10 wt. % of each type of compound were built in a $40 \times 40 \times 40$ Å^3 box with periodic

boundary condition. The ends of each compound were capped with hydrogen atoms. MD simulations were then conducted to equilibrate each system for 5.0 ns at 295 K. Correspondingly, we also built CG models of aqueous solutions for each type of bead and conducted similar MD simulations with adjusted the vdW parameters to match the RDFs obtained from the corresponding all-atom simulations.

To validate the CG parameters for bonded and nonbonded interactions in the hydrogel network, we constructed four other independent systems composed of aqueous solutions of single 37-mer poly(ethylene oxide) (PEO37), 16-mer polyglycine (GLY16), single PEGDA, and single $MethG_4RGDSP$ chains represented by both AA and CG models. Each of these solutions was built in a $40 \times 40 \times 40$ Å^3 box with periodic boundary condition and then equilibrated by a 60-ns MD simulation. The resulting chain conformations, which were characterized by the root-mean-square of the radius of gyration and end-to-end distance, were obtained from these simulations and then compared to assess how well the CG models were able to represent the all-atom behavior.

With the developed CG model parameters and the multiscale modeling toolset, we built CG models of 27 combinations of RGDSP-functionalized hydrogels (three tether lengths × nine peptide concentrations). The combination included three types of tether ($MethG_2RGDSP$, $MethG_4RGDSP$, and $MethG_6RGDSP$) and nine peptide concentrations (1.7, 3.4, 5.1, 6.8, 8.5, 10.2, 11.9, 13.6, and 15.3 mM) for each type of tether, which were selected to match the corresponding experimental studies for these PF-hydrogel systems.[12] With the multiscale modeling toolset, the initial polymer networks were generated by a MC method based on the on-lattice bond fluctuation model (BFM).[54,55] To approximate the nine molar concentrations of peptide from 1.7 to 15.3 mM, we designed nine model systems containing 1–9 MethGmRGDSP. Each of the nine model systems contains 533 PEGDA monomers; therefore, the molar ratio of MethG, RGDSP to PEGDA varies from about 0.002 to 0.017, which agrees with the ranged considered in experiment.[12]

In the MC simulations, the hydrogel surface structures were generated in orthogonal boxes with dimensions $88 \times 88 \times 25$. The total thickness of the surface was 50 lattice units. Periodic boundary conditions were imposed in the x-y plane, and a harmonic potential was imposed in the z-direction to restrain all chain segments to be sampled within the range of 50 lattice units in the z-direction to represent the top and bottom surfaces of the hydrogel.

The formation of a crosslinked polymer network in modeling was set up to be consistent to the crosslinking process used experimentally, i.e., each end of the PEGDA monomer or the methacrylated end of the peptide tether can be linked by two ends of other monomers. All monomers were initially aligned on the lattice in their completely extended states and then dynamically relaxed based on the BFM algorithm. Bond-angle-bending and bond-rotation energy terms obtained in the CG force field were imposed in the system potential energy during the MC procedure of network generation to guide the local configuration of the lattice chain segments close to their equilibrium state of the off-lattice CG model.[39] The crosslinking process was modeled as a collision process in which crosslinking happens when two linkable chain ends meet (the distance between them is 2, $\sqrt{5}$, $\sqrt{6}$, or 3 lattice units). For each system, after the degree of crosslinking between all monomers reached the 97%, the on-lattice sampling process was stopped, and the final configuration was recorded and prepared for a transition to the off-lattice model. This degree of crosslinking was selected because it is sufficiently high so that the small amount of crosslinking defects will not cause significant influence on the properties of the hydrogel systems in the simulations. To transfer the network structure from the lattice to the off-lattice models, the coordinates of the lattice points were scaled by a factor of 1.36 Å for length rescaling.[39] After transforming from the lattice model to the off-lattice CG model, the final dimensions of the crosslinked surface structures were about $120 \times 120 \times 68$ Å^3. With this volume, we obtained 1.7, 3.4, 5.1, 6.8, 8.5, 10.2, 11.9, 13.6, and 15.3 mM loadings of peptide for the three types of $MethG_mRGDSP$-functionalized hydrogels ($m = 2$, 4, and 6).

As a final step to form the hydrogels, each crosslinked surface structure was then immersed into a CG water box with dimensions $120 \times 120 \times 160$ Å^3. All water CG beads within 2.5 Å distance away from a solute bead were then removed to prevent CG-bead overlaps. Each hydrogel system with periodic boundary condition imposed in all directions was then energy minimized and then equilibrated with MD simulation for 50 ns. Since the molecular systems in modeling are much smaller in size than the actual systems in experiments, one specific network configuration in modeling is not able to represent the entire structure of a real hydrogel system but rather only represents a limited sampling of the actual material. Therefore, to improve the calculation accuracy, for each tether length and concentration in the hydrogel studied in this work, we prepared six independent initial configurations of each hydrogel system with the same degree of crosslinking and then calculated the ensemble average based on the six independent trajectories. Thus, 162 independent molecular systems of the PEG-based PF hydrogels were generated overall.

All simulations were conducted using the LAMMPS program.[56,57] For each individual system, four independent trajectories were generated using the MD method to improve the sampling efficiency. Each system was initially energy minimized for 2000 steps using the conjugate gradient method.[58] The MD simulations were then performed using the Nosé–Hoover algorithm[59,60] under constant volume and temperature conditions. Timesteps of 1.0 and 2.0 fs were used for simulations using the all-atom and CG models, respectively. For the AA simulations, covalent bonds involving hydrogen atoms were constrained using the SHAKE algorithm,[61] and the water molecules for the AA models were represented by the modified TIP3P water model for PCFF.[48] A dielectric constant value of 35, which resulted from the parameterization of the nonbonded interactions introduced in Sec. IV A, was used for all CG simulations.

For all simulations, the nonbonded vdW and electrostatic interactions were treated with real-space cutoffs of 12 and 10 Å, respectively.

IV. RESULTS AND DISCUSSION

A. Parameterization of coarse-grained model

The parameterization of the nonbonded interactions for water was conducted based on the standard Martini CG model of water,[46] in which four atomic water molecules are coarse-grained as a single bead (4:1) with neutral charge. The water bead defined in the standard Martini model has level I interaction strength with $\varepsilon = 1.195$ kcal/mol and $\sigma = 4.7$ Å.[46] The CG water parameters were developed based on PCFF in this work and the Martini parameters were used as an initial guess for parameter fitting. Specifically, we fixed the value of $\sigma = 4.7$ Å and iteratively adjusted the well depth ε until the calculated RDF profile converged to that given by Martini CG model of water. Figure 2 shows the converged mapping result of RDFs calculated by the CG models of water based on PCFF and standard Martini parameters.[47] The standard Martini neutral water model is substantially nonpolar and may cause water to freeze at room temperature. To prevent freezing, Marrink *et al.* introduced a small amount of "antifreeze" particles into the bulk of CG water to disturb the freezing process.[46] In the present work, we also mixed 1% antifreeze agents (bead type BP4) in WP4 waters to prevent freezing. The nonbonded parameters for the BP4 beads were quantified similar to the Martini model, in which σ was scaled up to 5.7 Å, and ε was set to about 1.12 times greater than the WP4 water bead. The parameters for the WP4 and BP4 beads are presented in Table I.

The parameterization of the ten types of CG beads included in the PF-hydrogel network was conducted based on 10 wt. % aqueous solutions of the small compounds presented in Fig. 1 that have similar atomic structures to the super-atom groups in their respective CG representation. Starting from the initial RDF obtained from atomistic calculations, the nonbonded interaction parameters were calculated by an iterative Boltzmann inversion scheme. For each of these CG beads, the electrostatic interaction was implicitly partitioned into the vdW interaction term. For each type of bead with neural charge, the parameters σ and ε were adjusted iteratively until the calculated RDF matched well with the corresponding AA result. For beads **R** and **D**, which represented positively and negatively charged segments, respectively, three parameters including σ, ε, and the value of the dielectric constant of water were all iteratively adjusted till the RDFs calculated by the CG models of aqueous solutions of pure **R** and **D** and their 1:1 mixture agreed well with the corresponding AA results. The results of σ and ε for all types of beads are presented in Table I. As examples, we show in Fig. 3 the results of RDFs calculated based on AA and CG models of aqueous solutions of **R** and **D** and their 1:1 mixture. In each plot, the RDFs from the CG simulations (open squares) reproduce the target distribution calculated by the AA model (lines) very well, with some deviations that are inherently due to the representation of asymmetric groups of individual atoms as spherically symmetric beads in the CG models.

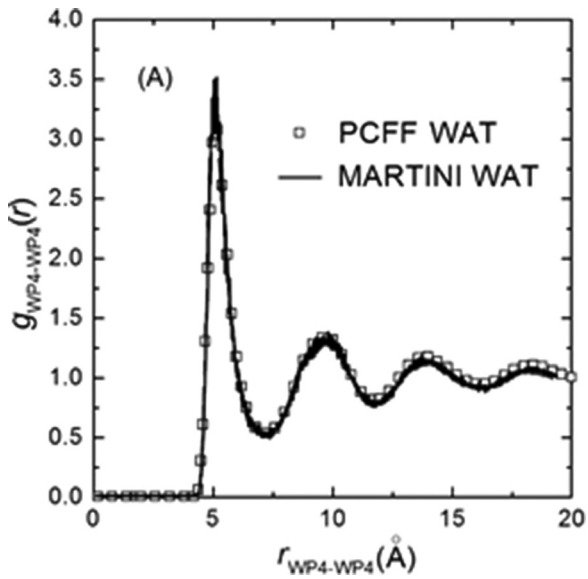

FIG. 2. Comparison of RDFs of CG water (WP4) calculated based on the standard Martini force field (Refs. 45 and 46) and PCFF.

The parameterization for the bonded interactions was conducted based on the AA simulations of the 29 types of 4-mer conformers in aqueous solution, from which the target probability distributions of various types of bond lengths, bond angles, and dihedral angles were determined and the initial guesses of bonded parameters of the CG force field were fitted based on Eqs. (1)–(3). The CG model parameters were then iteratively optimized by mapping the corresponding target profiles. The CG model parameters for 14 types of bond-stretching interactions, 20 types of bond-angle bending interactions, and 29 types of bond–rotation interactions are given in Tables II, III, and IV, respectively.

B. Simulation results for single chains

As shown in Fig. 1, the PEGDA crosslinker mainly contains ethylene-oxide segments corresponding to the predominant type of bead **C** in the CG model, and crosslinker $MethG_mRGDSP$ (m = 2, 4, and 6) mainly contains glycine segments corresponding to the predominant type of bead **G** in the CG model. Therefore, the accuracy of bonded and nonbonded CG parameters for these two types of beads is important for our simulations. AA and CG simulations were therefore first carried out to assess the behavior of aqueous solutions of single PEO37 and GLY16 chains for parameter validation, and then were carried out for aqueous solutions of single PEGDA and $MethG_4RGDSP$ crosslinkers which contain each type of CG bead for the further validation of the CG parameters. For all of these single chain aqueous solutions, we calculated the root-mean-square values of the end-to-end distances ($\langle R_e \rangle$) and the radius of gyration ($\langle R_g \rangle$) for each chain. Comparisons of these properties were then

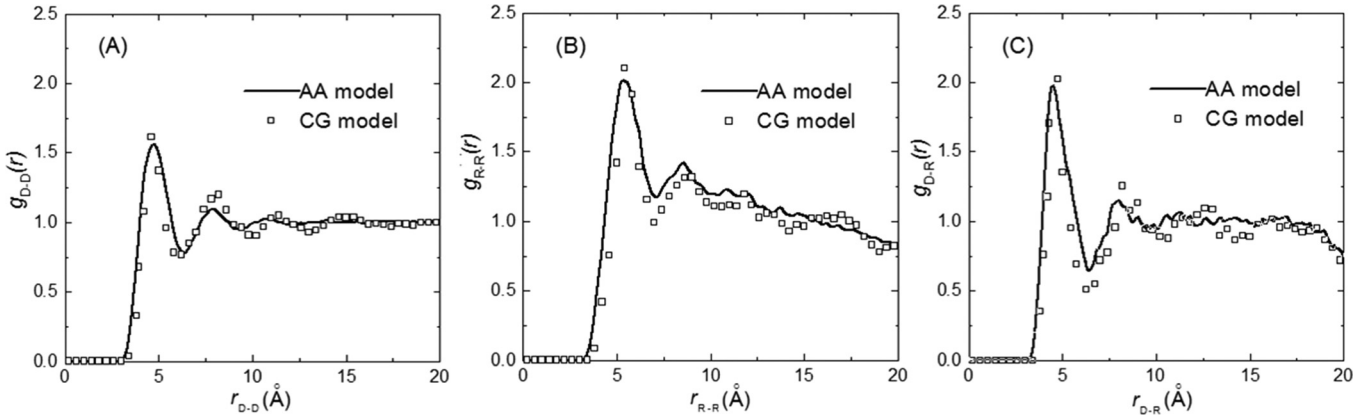

FIG. 3. Mapping results of the RDF obtained from the all-atom models and the CG models for beads ***R*** (A), ***D*** (B), and their 1:1 mixture (C).

made between the atomistic and the CG models. Figure 4 compares the distribution profiles of $\langle R_e \rangle$ calculated based on the AA (red lines) and CG (black lines) models for the different chains, and the ensemble averages of $\langle R_e \rangle$ and $\langle R_g \rangle$ obtained from these calculations are given in Table V. For PEO37, the CG results closely agree with both the AA results and the simulation results by Lee *et al*. based on the Martini CG force field.[32] There are no available published results of GLY16, PEGDA, or MethG$_4$RGDSP for comparison, but from the comparisons of the calculated chain conformation characterized by $\langle R_e \rangle$ and $\langle R_g \rangle$ for these chains, as presented in Table V, the CG results closely agree with the AA results for each chain in aqueous solution. These combined results show that the current CG models of the crosslinkers are able to accurately represent the behavior of the AA models of the crosslinkers in water, thus providing validation of the intrachain behavior for our CG parameter set developed based on PCFF.

C. Simulation results for RGDSP-functionalized hydrogels

1. Surface accessibility of the tethered peptides

In the experimental work of Jia *et al*.,[12] the RGDSP surface accessibility was characterized by the adhesion behavior of human adipose-derived stem cells (hADSCs) on the surface of hydrogel spots. The experimental results of Jia *et al*. are replotted in Fig. 5 for the MethG$_2$RGDSP-, MethG$_4$RGDSP-, and MethG$_6$RGDSP-functionalized hydrogels. The effects of RGDSP peptide concentration and tether length can be directly observed from the comparison of these results. For each type of tether, a small change of the peptide concentration is shown to cause significant changes in the cell attachment numbers over the low peptide concentrations, which we attribute to the increased surface accessibility of the peptide. Taking into account the rather large error bars, the cell adhesion results indicates that the cell attachment number becomes saturated after the peptide concentration increases up to about 6 mM for the MethG$_4$RGDSP and MethG$_6$RGDSP systems—but for the MethG$_2$RGDSP system, the cellular response has yet not saturated at this peptide concentration. The MethG$_4$RGDSP and MethG$_6$RGDSP systems show similar saturation numbers of attached cells and are about a factor of 2.5× greater than that of the MethG$_2$RGDSP system at 6 mM peptide concentration, suggesting that the longer tethers improve the accessibility of the peptide at the hydrogel surface.

Using the multiscale modeling toolset, we studied the accessibility of the RGDSP peptide at the surfaces of the hydrogels functionalized by MethG$_2$RGDSP, MethG$_4$RGDSP, and MethG$_6$RGDSP with different peptide concentrations in the hydrogel matrix. Figure 6 presents the evolution of the potential energy as a function of equilibration time for the

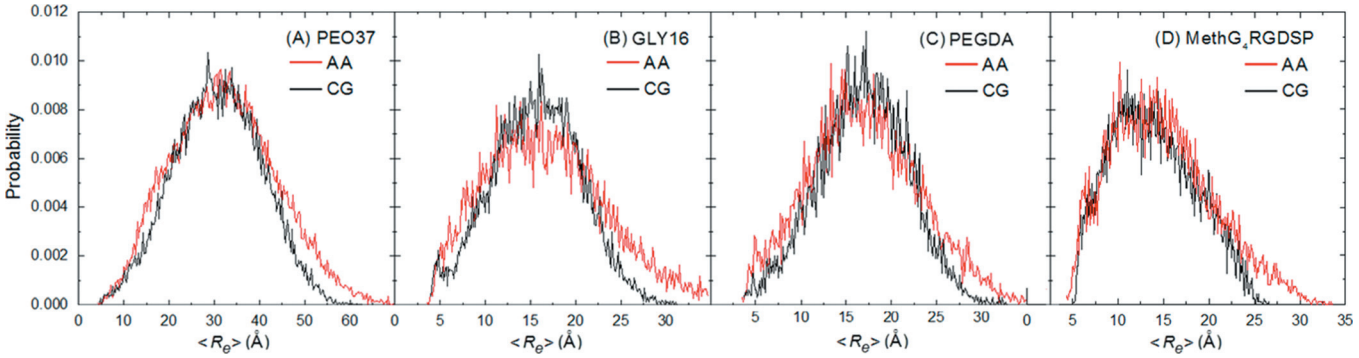

FIG. 4. All-atom (red line) and CG (black line) simulation results of root-mean-square end-to-end distance ($\langle R_e \rangle$) for PEO26, GLY16, PEGDA, and MethG$_4$RGDSP single chains in aqueous solution.

TABLE V. Comparison of all-atom and CG calculation results of the root-mean-square values of the end-to-end distance ($\langle R_e \rangle$) and radius of gyration ($\langle R_g \rangle$) of single PEO37, GLY16, PEGDA, and MethG_4RGDSP chains in aqueous solution.

	$\langle R_e \rangle$ (Å)		$\langle R_g \rangle$ (Å)	
Type	AA model	CG model	AA model	CG model
PEO37	31.635 ± 0.609	30.827 ± 0.466	13.318 ± 0.173	12.837 ± 0.104
GLY16	15.811 ± 0.198	15.742 ± 0.134	7.2981 ± 0.108	6.786 ± 0.056
PEGDA	16.566 ± 0.310	17.072 ± 0.198	6.8687 ± 0.086	6.953 ± 0.036
MethG_4RGDSP	13.667 ± 0.110	13.106 ± 0.168	6.643 ± 0.052	5.784 ± 0.033

15.3 mM MethG_4RGDSP functionalized hydrogel system, which provides indication that our system has equilibrated within 50-ns of sampling. Figure 7 presents a typical configuration of the MethG_4RGDSP functionalized hydrogel structure represented by the CG models, in which the beads colored red, green, and copper represent the tethered peptide, hydrogel matrix, and crosslinked chain ends, respectively, and the light blue dots represent the water in the system. To define the position of the hydrogel surface, we calculated the density distribution for the CG beads contained in the PEGDA hydrogel matrix for x-y planes as a function the z-coordinate, with the x-y planes being parallel to the hydrogel surface and the z-coordinate direction being normal to the surface. The normalized density probability profile of the PEGDA beads is plotted in Fig. 8, in which the average surface position is determined at 0.5 probability density compared to the bulk hydrogel matrix. As shown in Fig. 8, the surface plane is thus designated to be located at $|z - z_c| = 40$ Å, where z is the coordinate in the direction normal to the surface plane and z_c is the position of the midplane of the hydrogel matrix.

To estimate the surface accessibility of the peptide, we calculated the distribution of the center of mass of the RGDSP segments in the direction normal to the surface. Figures 9(a)–9(c) present the effects of peptide concentration on the surface accessibility of the RGDSP peptide with G2, G4 and G6 linker, respectively. The effect of tether length on the surface accessibility of peptide is presented in Fig. 10. In each figure, the normalized density distribution profile of the center of mass of RGDSP is plotted as a function of the distance away from the center of the hydrogel. Figure 9 shows that as the concentration increases for the MethG_mRGDSP (m = 2, 4, and 6) system, instead of being evenly distributed within the hydrogel matrix, the peptides are shown to increasingly partition themselves to be positioned at the hydrogel surface, thus increasing their surface accessibility as needed for cell–receptor binding. This behavior thus indicates that, thermodynamically, the tethered peptide has a tendency to phase separate from the hydrogel matrix and be preferentially concentrated at the hydrogel–water interface. Figure 10 shows the effect of the tether length on the peptide accessibility at the hydrogel surface as a composite for all peptide concentrations with the designated tether length. This figure shows clearly that, in the systems with short tethers (G_2), the peptides are mainly partitioned inside the bulk of the hydrogel matrix with the G_2 tether not being sufficiently long to enable the peptide to concentrate at the hydrogel surface. In contrast, with the longer tethers (G_4 and G_6), the peptides are much more able to partition themselves away from the bulk of the hydrogel and move toward to the surface region, thus showing their thermodynamic preference for the hydrogel–water interface. As shown in Fig. 10, the density probability profiles for the G_4 and G_6 tether lengths are quite similar.

For the three types of tether lengths, we also calculated the average height of the center of mass of the RGDSP

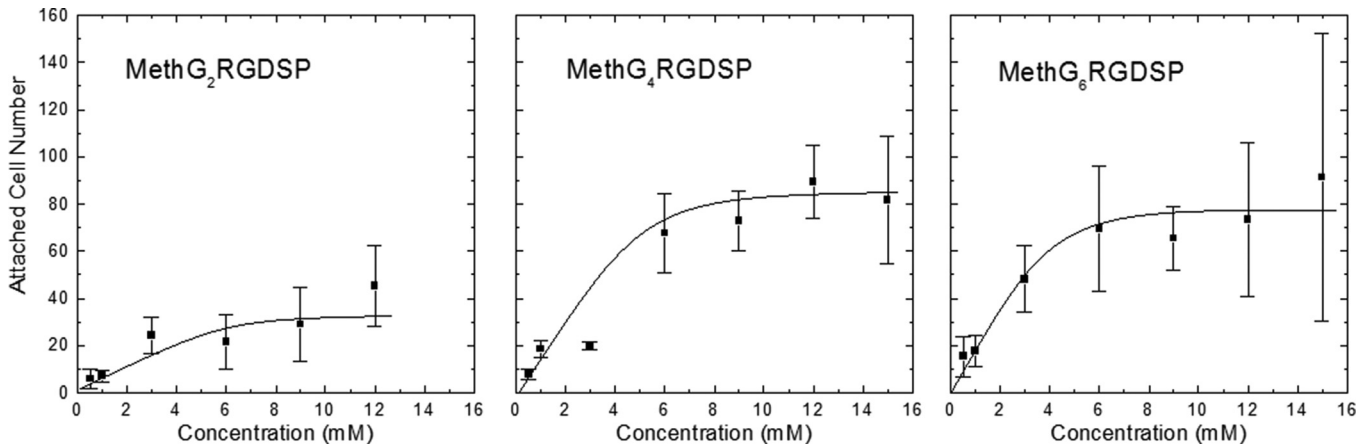

FIG. 5. Experimental measurements of the average number of hADSCs cells attached on the surface of MethG_mRGDSP (m = 2, 4, and 6) peptide-functionalized hydrogels as a function of the concentration of the RGDSP peptide in the hydrogel matrix. [Reproduced with permission from Jia *et al.*, Acta Biomater. **45**, 110 (2016). Copyright 2016 by Elsevier.]

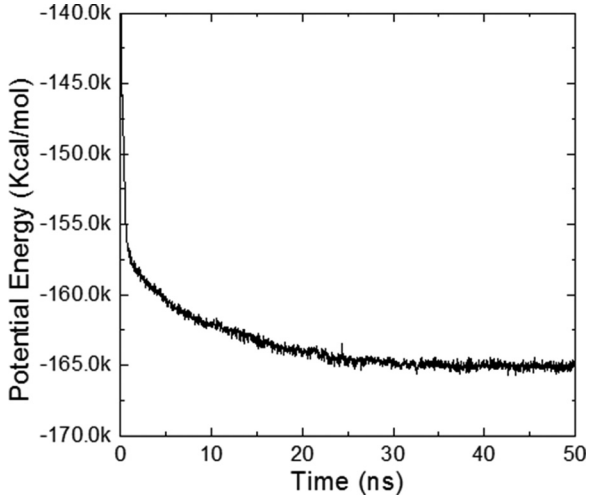

FIG. 6. Evolution of the potential energy obtained from 50 ns 15.3 mM $MethG_4RGDSP$ simulation.

peptides for the peptides that extended past the defined hydrogel surface plane (i.e., $|z - z_c| = 40$ Å); these results are presented in Fig. 11. As shown, the average heights of the RGDSP peptides above the surface for each of the different hydrogel systems are very similar. These results further reflect the behavior shown in Figs. 9 and 10 that the tethered peptides tend to be thermodynamically partitioned at the hydrogel–water interface and do not tend to extend out from this interface into the bulk aqueous solution. This behavior suggests that tether type used to link the peptide to the hydrogel matrix (i.e., a series of glycines) may be too hydrophobic to actually escape from the hydrogel and extend into the surrounding aqueous solution. Based on these results, we propose that a more hydrophilic tether may improve the bioactivity of the hydrogels by enabling the tethered peptides to extend further beyond the hydrogel surface and into the surrounding aqueous solution, which should make them more accessible for cell–receptor binding.

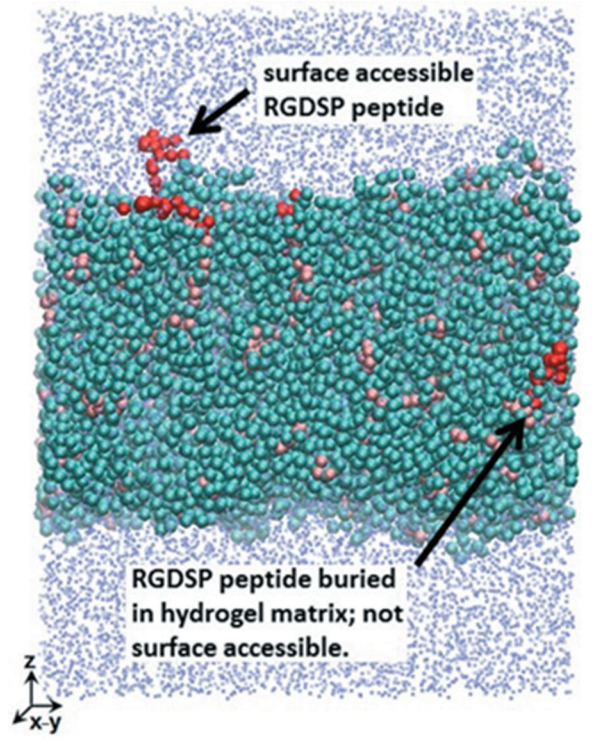

FIG. 7. Example configuration of the $MethG_4RGDSP$ functionalized hydrogel surface structure represented by CG model, in which the beads in red, blue, copper, and light blue color represent the tethered peptide, matrix, crosslinked chain ends, and waters in the system, respectively. The plots were created by the VMD program (Ref. 63).

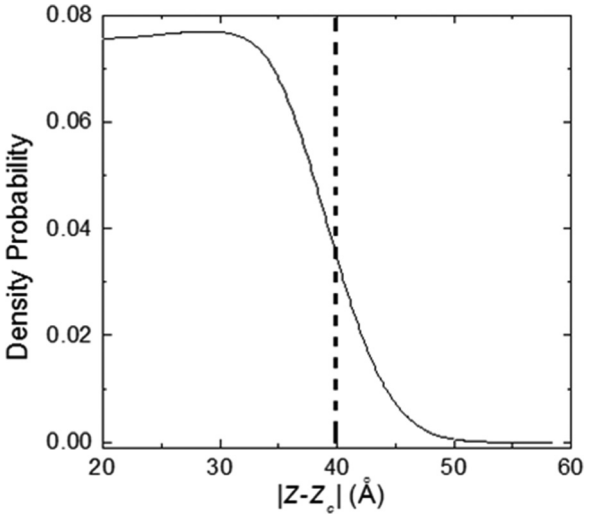

FIG. 8. Normalized probability density of the PEGDA beads. The surface position, $|z - z_c| = 40$ Å, is determined at 0.5 density probability, where z is the coordinate in direction normal to the surface and z_c is the position of the midplane of the hydrogel matrix.

The results of the effects of peptide concentration and tether length on the surface accessibility of the peptide are consistent with the experimental observations[12] shown in Fig. 5. Before saturation of cell attachment (Fig. 5), the attached number of cells increased as the concentration of peptide increased and the increase was more rapid for the longer tether systems. It is interesting to observe that, consistent with the modeling results shown in Figs. 9, 10, and 11, the G_4 and G_6 systems in the experimental results showed very similar behaviors in cell adhesion.

2. Orientation of the tethered peptides at the hydrogel surface

The asymmetry parameter, which indicates the average orientation relative to a reference direction, is a useful measure of the orientation of the tether–peptide construct near the hydrogel surface. Using a reference direction, z, which is normal to the surface, the asymmetry parameter, λ_z, is defined by[62]

$$\lambda_z = \frac{2\langle R_{gz}^2\rangle_z - \langle R_{gx}^2\rangle_z - \langle R_{gy}^2\rangle_z}{2\left(\langle R_{gx}^2\rangle_z + \langle R_{gy}^2\rangle_z + \langle R_{gz}^2\rangle_z\right)}, \quad (6)$$

where $\langle R_{gs}{}^2\rangle_z$ $(s = x, y, z)$ denotes the s component of the mean-square radius-of-gyration tensor of a tethered peptide

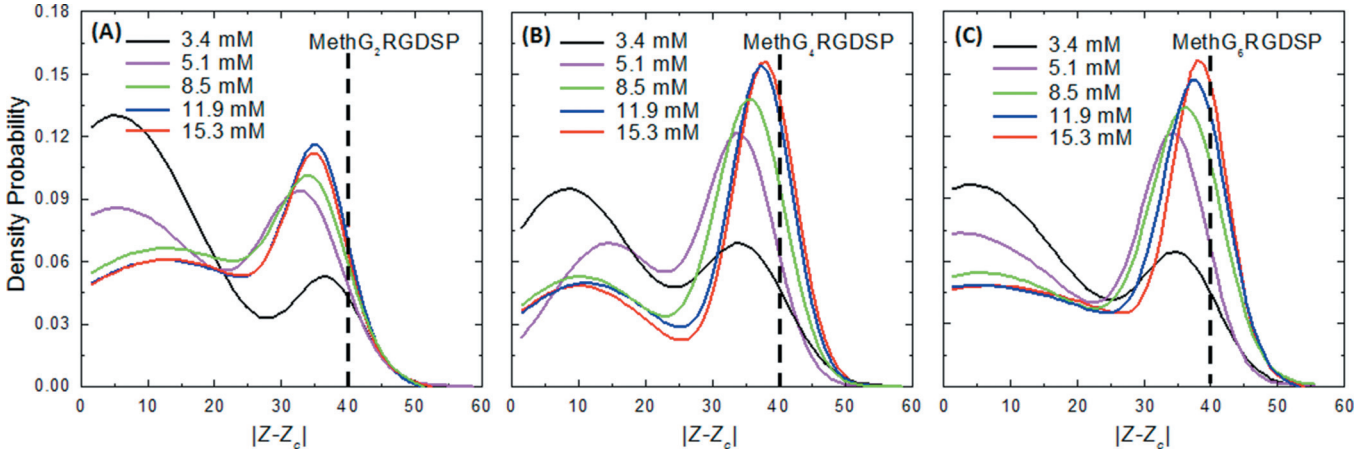

FIG. 9. Effects of peptide concentration on the normalized probability density distribution of RGDSP peptide with the designated tether length, i.e., G2, G4, and G6. The dashed line at $|z - z_c| = 40$ Å indicates the position of the hydrogel surface.

at position z. Physically, $\lambda_z = 1$ represents an orientation perfectly perpendicular to the hydrogel surface, and $\lambda_z = -0.5$ indicates an orientation perfectly parallel with respect to the surface plane of the hydrogel. A 45° or completely random orientation results in λ_z being 0.00. The changes of the asymmetry parameters as a function of distance from the center of the hydrogel matrix are presented in Fig. 12 for the $MethG_2RGDSP$, $MethG_4RGDSP$, and $MethG_6RGDSP$ hydrogels. These plots show that, in general, the average value of λ_z within the hydrogel matrix below the surface plane (i.e., $|z - zc| \leq 40$ Å) tends to slightly increase as the length of the tether increases, indicating an increasing tendency to orient normal to the surface of the hydrogels that are functionalized with the longer tethers. This behavior goes along with the tendency of the tethered peptide to preferentially phase separate from the bulk hydrogel matrix and extend toward the surface of the hydrogel, as shown in Figs. 9 and 10. At the surface (or the interfacial region between the hydrogel matrix and surrounding bulk water; around $|z - z_c| = 40$ Å), the values of λ_z show a dramatic difference between the tether lengths. In this region, above the hydrogel surface plane (i.e., $|z - z_c| > 40$ Å), the G_2 system exhibits a fairly random orientation. In contrast, the G_4 system shows strong preference to orient more perpendicular to the surface, which can be considered to position the tethered peptide in an orientation that should be more amenable for cell signaling. The longer-tethered G_6 systems, however, exhibits a rather deep minimum just above the hydrogel surface plane, which indicates a strong tendency to orient itself more parallel to the surface before tending to then turn slightly more perpendicular as it extends further from the surface plane. The orientation behavior of the $MethG_6RGDSP$ tethers at the surface thus indicates that, compared to $MethG_4RGDSP$, the two additional glycine linkers in $MethG_6RGDSP$ cause stronger interaction with the molecular environment formed at the hydrogel–water interface, which may be considered more likely to inhibit the ability of the tethered peptide to be positioned in a manner that is needed for effective cell–receptor recognition. Although speculative at this time, this may explain the much greater variance in the cell binding response (i.e., longer error bars) observed experimentally for the $MethG_6RGDSP$ system compared to the $MethG_4RGDSP$ system as presented in Fig. 5.

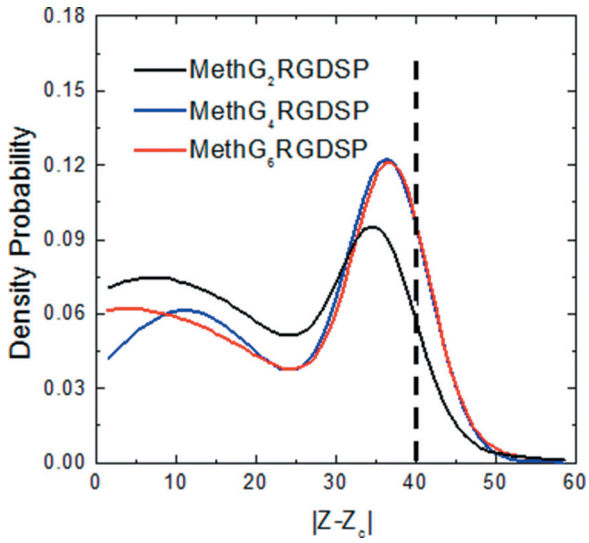

FIG. 10. Effects of tether length on the normalized probability density distribution of RGDSP peptide as a composite for all peptide concentrations with the designated tether length. The dashed line at $|z - z_c| = 40$ Å indicates the position of the hydrogel surface.

3. Surface density of the tethered peptides

The overall surface density of the RGDSP peptide is another important quantity in determining its accessibility for cell–receptor binding to the hydrogel surface, with a critical peptide surface density likely being required to achieve a saturation level of cell attachment, as indicated in the experimental data plots for cell binding versus peptide concentration shown in Fig. 5.

For each simulated hydrogel system, the surface density, ρ_s, was therefore calculated as

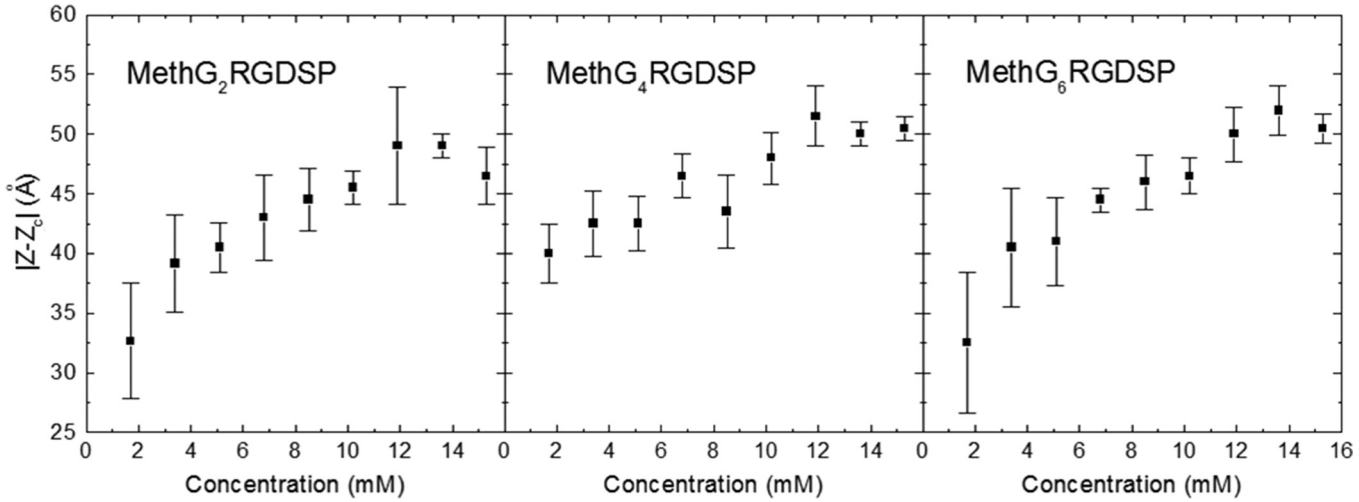

FIG. 11. Effects of peptide concentration and tether length on the average height that the center of mass of the RGDSP peptides can reach beyond the average hydrogel surface position. Each data point was averaged over 24 independent trajectories. The error bars represent the standard deviation.

$$\rho_S = \frac{\langle n_{\mathrm{RGDSP}} \rangle}{S}, \tag{7}$$

where $\langle n_{\mathrm{RGDSP}} \rangle$ is the average mole number of RGDSP segments with the z-coordinate of the center of mass having a position of $|z - z_c| \geq 40$ Å, and $S = 120 \times 120$ Å^2 is the surface area of the modeled hydrogel system.

The calculated surface densities as a function of RGDSP concentration are presented in Fig. 13 for the $MethG_2RGDSP$-, $MethG_4RGDSP$-, and $MethG_6RGDSP$-functionalized hydrogel systems, respectively. The straight solid line in each figure represents the linear fitting result. In general, the calculated values of ρ_s of the two longer tether systems ($MethG_4RGDSP$ and $MethG_6RGDSP$) are greater than those of the shortest tether system ($MethG_2RGDSP$) for each concentration of the peptide, indicating that the longer tether lengths are better able to present the peptide at the hydrogel surface. Again, similar ρ_s values are found for both the $MethG_4RGDSP$ and $MethG_6RGDSP$ systems, which shows agreement with the experimental data on the cellular adhesion response plotted in Fig. 5. As shown in Fig. 13, the linear fitting results in similar slope [0.003 (μmol/m^2)/mM] for both of these systems. Based on the experimentally measured cell adsorption data (Fig. 5) and the calculated surface density results, we are able to predict the required critical surface density of peptide to saturate the cellular adhesion response on the hydrogel surfaces. Specifically, it is observed experimentally in Fig. 5 that cell adhesion saturation happened on the surface of the $MethG_4RGDSP$ and $MethG_6RGDSP$ hydrogels for about 6 mM peptide concentration (corresponding to the beginning of the plateau region of the fitted sigmoidal curves). From Fig. 11, the corresponding surface density at 6 mM peptide concentration is about 0.016 μmol/m^2 (horizontal dashed line). Based on this value representing the critical surface density of the peptide needed to maximize the cellular adhesion response, our simulation results can thus provide guidance for the design of other similar PF-hydrogel systems. By combining the data sets obtained from Figs. 5 and 13, the cell adhesion number obtained from experiment can be plotted

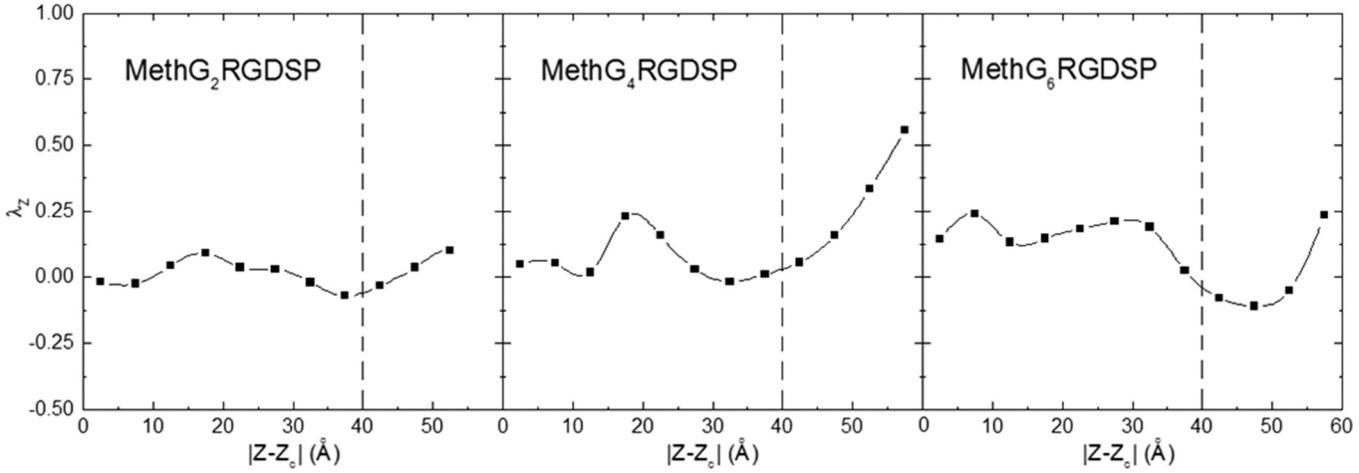

FIG. 12. Effects of peptide concentration and tether length on the asymmetry parameter of the tethers as a function of distance from the midplane of the hydrogel. The dashed line at $|z - z_c| = 40$ Å indicates the position of the hydrogel surface.

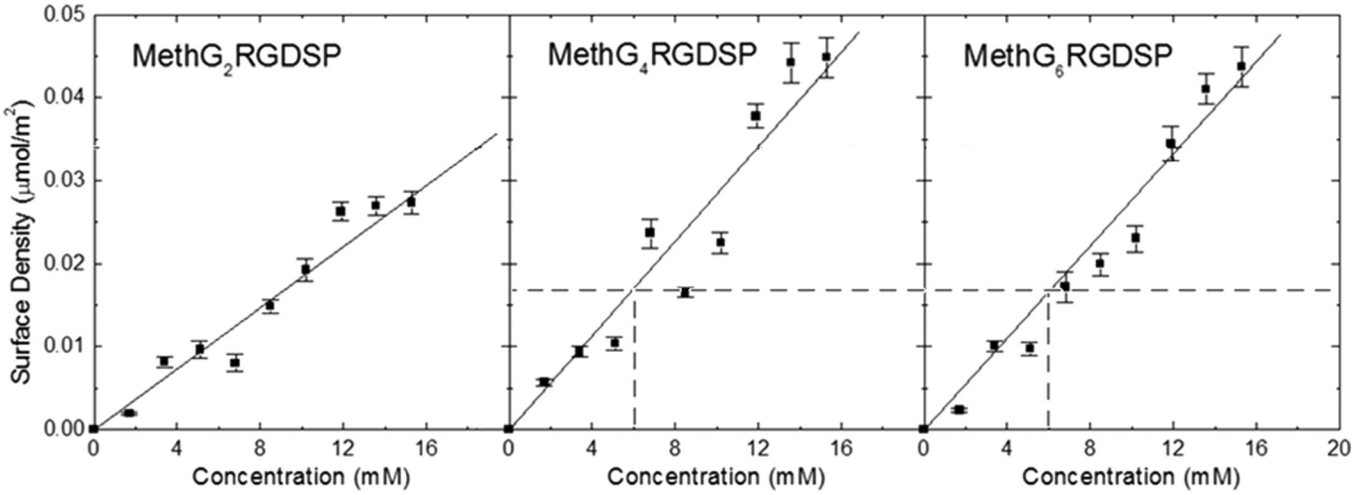

FIG. 13. RGDSP surface concentration for hydrogels with different peptide loadings and tether lengths. The horizontal dashed line indicates the critical surface concentration for saturated cell adhesion to the hydrogel surface, which is determined by the $MethG_4RGDSP$ and $MethG_6RGDSP$ results. Each data point was averaged over 24 independent trajectories. The error bars represent the standard deviation.

versus the peptide surface concentration density obtained from simulation for each peptide loading in the hydrogel (Fig. 14). As clearly shown from this plot, the G_4 and G_6 tether lengths provide substantially greater cell adhesion than the G_2 tether length for a given peptide surface concentration, thus indicating that the longer tether lengths present the peptide in a manner that is more conducive to cell adhesion. Figures 13 and 14 thus demonstrate examples of how results from the molecular simulations can provide insights into the molecular behavior of the PF-hydrogels that influence their bioactivity that cannot be obtained by the experimental studies alone.

V. CONCLUSIONS

In this work, we have developed CG models for peptide-functionalized hydrogels formed from PEGDA and $MethG_mRGDSP$ crosslinkers for Gly-tether lengths of $m = 2$, 4, and 6. A combination of the CG model and a multiscale modeling method enabled us to investigate the accessibility of the peptides at the surface of the hydrogels. Based on the ensemble of states generated in the simulations for the 27 combinations of PF-hydrogels (3 tether lengths $\times$ 9 peptide concentrations), the effects of peptide concentration and tether length on the peptide surface accessibility have been examined.

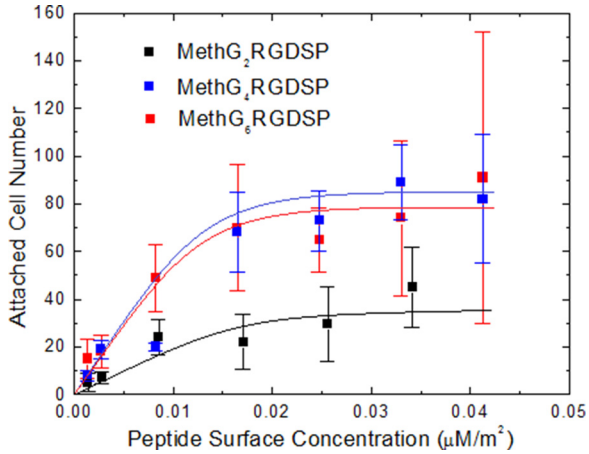

FIG. 14. Cell adhesion number (obtained from experiment) [Reproduced with permission from Jia *et al.*, Acta Biomater. **45**, 110 (2016). Copyright 2016 by Elsevier] vs the peptide surface concentration density (obtained from simulation) for each peptide loading and tether length in the hydrogel. This gives an example of how the simulation provides insights of molecular behavior to explain the experimental observations.

Our studies indicate that for this PF-hydrogel system, as the peptide concentration and the length of tether increase, the peptides tend to thermodynamically partition away from the bulk phase of the hydrogel and move toward the surface region. The results further show that, using sequences of the relatively hydrophobic glycine amino acid for the tether, the tethered peptides tend to concentrate at the hydrogel–water interface rather than extending further out into the surrounding aqueous solution as the tether length is increased from four to six glycines. Based on the assumption that better cell–receptor accessibility will be provided as the peptide is able to extend further from the hydrogel surface and out into the surrounding aqueous solution, these results thus suggest that use of a more hydrophilic tether may improve the performance of this PEGDA-$MethG_mRGDSP$ hydrogel system.

For the hydrogel systems studied in this work, the probability density of the tethered peptide for the $MethG_4RGDSP$ and $MethG_6RGDSP$ hydrogels were quite similar, with these systems both providing enhanced surface accessibility compared to the $MethG_2RGDSP$ system for a given peptide concentration. These simulation results agree very well with the corresponding available experimental cell adhesion measurements. In addition to the distribution of the peptide in the hydrogel, the simulations also enabled us to predict the orientation and the surface concentration of the peptide at the surface of the hydrogel as well as the critical surface concentration required to attain maximum cellular adhesion. We propose that each of these metrics provides important parameters for characterizing and understanding PF-hydrogel structure and subsequent bioactivity.

In conclusion, the multiscale modeling toolset developed in our series of studies has been successfully applied to characterize the molecular structure of a specific type of PF-hydrogel. The simulation methods combined with the CG models are able to efficiently predict the structure and bioactivity of the PF-hydrogels. We propose that these methods have the potential to provide a powerful new tool for hydrogel design for tissue engineering and regenerative medicine to optimize cellular response.

ACKNOWLEDGMENTS

This work was supported by "RESBIO—The National Resource for Polymeric Biomaterials" funded under NIH Grant No. P41 EB001046-01A1 with additional support provided by NIH NIGMS IDeA Grant No. P20GM103444, and the Center for Advanced Fibers and Films (CAEFF) at Clemson University. Computational support was provided by the Palmetto High Performance Computing Resource at Clemson University.

[1]M. P. Lutolf and J. A. Hubbell, Nat. Biotechnol. **23**, 47 (2005).
[2]W. Tang and M. L. Becker, Chem. Soc. Rev. **43**, 7013 (2014).
[3]L. Bedian, A. M. Villalba-Rodríguez, G. Hernández-Vargas, R. Parra-Saldivar, and H. M. N. Iqbal, Int. J. Biol. Macromol. **98**, 837 (2017).
[4]S. Ahadian, R. B. Sadeghian, S. Salehi, S. Ostrovidov, H. Bae, M. Ramalingam, and A. Khademhosseini, Bioconjug Chem. **26**, 1984 (2015).
[5]R. Censi, P. Di Martino, T. Vermonden, and W. E. Hennink, J. Controlled Release **161**, 680 (2012).
[6]E. Jabbari, Curr. Opin. Biotechnol. **22**, 655 (2011).
[7]J. Y. Shu, B. Panganiban, and T. Xu, Annu. Rev. Phys. Chem. **64**, 631 (2013).
[8]A. M. Moursi, C. H. Damsky, J. Lull, D. Zimmerman, S. B. Doty, S. Aota, and R. K. Globus, J. Cell. Sci. **109**, 1369 (1996).
[9]E. Ruoslahti and M. D. Pierschbacher, Cell **44**, 517 (1986).
[10]N. M. Moore, N. J. Lin, N. D. Gallant, and M. L. Becker, Acta Biomater. **7**, 2091 (2011).
[11]D. L. Hern and J. A. Hubbell, J. Biomed. Mater. Res. **39**, 266 (1998).
[12]J. Jia, R. C. Coyle, D. J. Richards, C. L. Berry, R. W. Barrs, J. Biggs, C. J. Chou, T. C. Trusk, and Y. Mei, Acta Biomater. **45**, 110 (2016).
[13]F. A. Escobedo and J. J. de Pablo, Phys. Rep. **318**, 85 (1999).
[14]T. Tonsing and C. Oldiges, Phys. Chem. Chem. Phys. **3**, 5542 (2001).
[15]I. Yarovsky and E. Evans, Polymer **43**, 963 (2002).
[16]N. Nima and Z. R. Saeed, Macromolecules **44**, 5481 (2011).
[17]I. Atsushi, N. Toshio, and S. Mitsuhiro, Soft Matter **8**, 5283 (2012).
[18]J. R. Saunders, S. Abu-Salih, T. Khaleque, S. Hanula, and W. Moussa, J. Comput. Theor. Nanosci. **5**, 1942 (2008).
[19]E. R. Duering, K. Kremer, and G. S. Grest, J. Chem. Phys. **101**, 8169 (1994).
[20]I. Taketo, T. Makoto, K. Masayuki, and T. A. Tomoo, Chem. Lett. **40**, 309 (2011).
[21]Y. R. Sliozberg, R. A. Mrozek, J. D. Schieber, M. Kröger, J. L. Lenhart, and J. W. Andzelm, Polymer **54**, 2555 (2013).
[22]Q. F. Wang, D. J. Keffer, S. X. Deng, and J. Mays, J. Phys. Chem. C **117**, 4901 (2013).
[23]Q. F. Wang, D. J. Keffer, S. X. Deng, and J. Mays, Polymer **53**, 1517 (2012).
[24]M. Schulz and J. U. Sommer, J. Chem. Phys. **96**, 7102 (1992).
[25]J. U. Sommer, Macromol. Symp. **81**, 139 (1994).
[26]F. A. Escobedo and J. J. de Pablo, J. Chem. Phys. **104**, 4788 (1996).
[27]S. Nedelcu and J. U. Sommer, J. Chem. Phys. **130**, 204902 (2009).
[28]P. Kosovan, T. Richter, and C. Holm, *Intelligent Hydrogels*, Progress in Colloid and Polymer Science, edited by G. Sadowski and W. Richtering (Springer, Switzerland, 2013), Vol. 140, p. 205.
[29]T. Y. Sun, L. J. Liang, Q. Wang, A. Laaksonen, and T. Wu, Biomater. Sci. **2**, 419 (2014).
[30]E. Chiessi, F. Cavalieri, and G. Paradossi, J. Phys. Chem. B **111**, 2820 (2007).
[31]J. Walter, J. Sehrt, J. Vrabec, and H. Hasse, J. Phys. Chem. B **116**, 5251 (2012).
[32]H. Lee, A. H. de Vries, S. J. Marrink, and R. W. Pastor, J. Phys. Chem. B **113**, 13186 (2009).
[33]W. Shinoda, R. DeVane, and M. L. Klein, J. Phys. Chem. B **114**, 6836 (2010).
[34]W. Shinoda, R. DeVane, and M. L. Klein, Mol. Simul. **33**, 27 (2007).
[35]W. Shinoda, R. DeVane, and M. L. Klein, Soft Matter **4**, 2454 (2008).
[36]T. I. Ergenc and S. Kizilel, "Recent advances in the modeling of PEG hydrogel membranes for biomedical applications," in *Biomedical Engineering, Trends in Material Science*, edited by N. L. Anthony (InTech, 2011), Chap. 14.
[37]D. Zanuy, I. W. Hamley, and C. Alemán, J. Phys. Chem. B **115**, 8937 (2011).
[38]"Lattice models," http://www.tcm.phy.cam.ac.uk/~tmf20/PHYSICS/thesis/node18.html.
[39]X. F. Li, N. S. Murthy, M. L. Becker, and R. A. Latour, Biointerphases **11**, 021002 (2016).
[40]P. C. Hariharan and J. A. Pople, Theor. Chim. Acta **28**, 213 (1973).
[41]M. M. Francl, W. J. Pietro, W. J. Hehre, J. S. Binkley, M. S. Gordon, D. J. DeFrees, and J. Pople, J. Chem. Phys. **77**, 3654 (1982).
[42]U. Dinur and A. T. Hagler, *Reviews in Computational Chemistry*, edited by K. B. Lipkowitz and D. B. Boyd (VCH, New York, 1991), Vol. 2, pp. 99–164.
[43]J. R. Maple, M. J. Hwang, T. P. Stockfisch, U. Dinur, M. Waldman, C. S. Ewig, and A. T. Hagler, J. Comput. Chem. **15**, 162 (1994).
[44]S. Kmiecik, D. Gront, M. Kolinski, L. Wieteska, A. E. Dawid, and A. Kolinski, Chem. Rev. **116**, 7898 (2016).
[45]G. D'Adamo, A. Pelissetto, and C. Pierleoni, Soft Matter **8**, 5151 (2012).
[46]S. J. Marrink, J. Risselada, S. Yefimov, D. P. Tieleman, and A. H. de Vries, J. Phys. Chem. B **111**, 7812 (2007).
[47]S. O. Yesylevskyy, L. V. Schäfer, D. Sengupta, and S. J. Marrink, PLoS Comput. Biol. **6**, e1000810 (2010).
[48]L. Fritz and D. Hofmann, Polymer **38**, 1035 (1997).
[49]D. Reith, H. Meyer, and F. Müller-Plathe, Macromolecules **34**, 2335 (2001).
[50]W. Tschöp, K. Kremer, J. Batoulis, T. Bürger, and O. Hahn, Acta Polym. **49**, 61 (1998).
[51]X. F. Li and R. A. Latour, Polymer **50**, 4139 (2009).
[52]E. M. Ahmed, J. Adv. Res. **6**, 105 (2015).
[53]M. Waldman and A. T. Hagler, J. Comput. Chem. **14**, 1077 (1993).
[54]J. S. Shaffer, J. Chem. Phys. **101**, 4205 (1994).
[55]I. Carmesin and K. Kremer, Macromolecules **21**, 2819 (1988).
[56]S. Plimpton, J. Comput. Phys. **117**, 1 (1995).
[57]"LAMMPS molecular dynamics simulator," http://lammps.sandia.gov.
[58]M. R. Hestenes and E. Stiefel, J. Res. Natl. Bur. Stand. **49**, 2379 (1952).
[59]S. Nosé, Mol. Phys. **52**, 255 (1984).
[60]W. G. Hoover, Phys. Rev. A **31**, 1695 (1985).
[61]W. F. van Gunsteren and H. J. C. Berendsen, Mol. Phys. **34**, 1311 (1977).
[62]M. Müller, K. Binder, and W. Oed, J. Chem. Soc. Faraday Trans. **91**, 2369 (1995).
[63]W. Humphrey, A. Dalke, and K. Schulten, J. Mol. Graphics **14**, 33 (1996).